Particle Image Velocimetry Experiments and Direct Numerical Simulations of Solids Suspension in Transitional Stirred Tank Flow

Genghong Li[a,b,c], Zhipeng Li[a,b,*], Zhengming Gao[a,b,*], Jiawei Wang[a,b], Yuyun Bao[a,b], J. J. Derksen[c]

a Beijing Advanced Innovation Center for Soft Matter Science and Engineering, Beijing University of Chemical Technology, Beijing 100029, China

b State Key Laboratory of Chemical Resource Engineering, School of Chemical Engineering, Beijing University of Chemical Technology, Beijing 100029, China

c School of Engineering, University of Aberdeen, Aberdeen AB24 3UE, UK

Corresponding author

E-mail address: lizp@mail.buct.edu.cn (Zhipeng Li), gaozm@mail.buct.edu.cn (Zhengming Gao);

Tel: +8610 64418267;

Fax: +8610 64449862;

Mailbox 230, School of Chemical Engineering,

Beijing University of Chemical Technology, Beijing, 100029, China.

Abstract

Solids suspension in a stirred tank with a down-pumping pitched-blade turbine impeller has been investigated by using particle image velocimetry (PIV) experiments as well as direct numerical simulations (DNS) with a lattice-Boltzmann (LB) method. The flow regime of this solid-liquid two-phase system is transitional with the impeller-based Reynolds numbers Re = 1334. The refractive index matching (RIM) method is applied in the experiments. The overall solids volume fractions are up to 8% in the experiments as well as in the simulations. The liquid flow fields around the particles are highly resolved in both experimental and simulated cases which makes it possible to investigate solid-liquid interactions in detail. The average distributions of the solids over the tank volume as predicted by the simulations are in good agreement with the experimental results. It is shown that the presence of particles reduces the average velocities as well as the turbulent fluctuation levels of the liquid in both the experiments and simulations although the reduction in the simulations is weaker as compared to in the experiments.

Keywords: solid-liquid suspension, stirred tank, particle image velocimetry, refractive index matching, lattice-Boltzmann method

1. Introduction

Solid-liquid stirred tanks are very common in industrial processes such as biopharmaceutical reactors, catalytic chemical reactors and agitated crystallization reactors. In most cases, the flow regime in these reactors is either laminar (Mo et al., 2015) or turbulent (Li et al., 2018). However operation under transitional flow (Zhang et al., 2017) conditions are receiving more and more attention. For instance when scaling up from bench scale to pilot scale, results obtained for transitional flow at bench scale need to be carefully interpreted before applying them to – fully turbulent – pilot scale conditions. Furthermore, solid-liquid two-phase flows are more complicated compared to single-phase liquid flows because the strong dynamical coupling between solids and liquid. Therefore, it is important to investigate the process of solid-liquid suspension in stirred tanks with transitional flows with an emphasis on the way liquid and solids interact.

There are many investigations about solid-liquid suspension in stirred tanks of an experimental as well as numerical nature. As for the experiments, Zwietering (1958) first proposed the seminal concept of just-suspended impeller speed N_{js}, which is defined as the impeller speed at which no particles remain still on the base of the tank for more than 1-2 s. Based on this criterion, some researchers (Nienow, 1968; Baldi et al., 1978; Sharma and Shaikh, 2003; Angst and Kraume, 2006; Bittorf and Kresta, 2003; Sardeshpande et al., 2011) proposed various N_{js} correlations for stirred tanks with different geometric constructions or different flow configurations. The power dissipated (Nienow, 1968; Baldi et al., 1978; Sharma and Shaikh, 2003; Angst and Kraume, 2006) as well as the solids cloud height (Bittorf and Kresta, 2003; Sardeshpande et al., 2011) were also measured in stirred tanks. Besides these global dynamic characteristics of solids suspension processes, many local properties have been investigated. Guha et al. (2007) used a non-intrusive experimental technique - computer automated radioactive particle tracking - to obtain the time-averaged velocities and the turbulent quantities of the solids flow field in dense solid-liquid suspensions. Guida et al. (2009, 2010) used positron emission particle tracking, which also is a non-intrusive technique, to determine the full 3D velocity and concentration fields of the solids as well as of the liquid. Electrical resistance tomography is another non-intrusive flow visualization technique. It has been used to investigate how impeller type, impeller diameter, impeller speed, impeller off-bottom clearance, particle sizes and solids volume fractions affect the distribution and homogeneity of solids in stirred tanks (Hosseini et al., 2010; Carletti et al., 2014; Tahvildarian et al., 2011; Harrison et al., 2012)

When it comes to investigations of liquid flow field in the stirred tanks, laser-based techniques such as Particle Image Velocimetry (PIV) (Virdung and Rasmuson, 2007a; Unadkat et al., 2009; Gabriele et al., 2011; Montante et al., 2012) and Laser

Doppler Anemometry (LDA) (Guiraud et al., 1997; Micheletti and Yianneskis, 2004; Virdung and Rasmuson, 2007b) have been widely used. Optical accessibility is a major limiting factor when applying such techniques to solid-liquid two-phase systems, especially those with high solids loadings. The presence of particles will obstruct and scatter the laser light which will render results of poor quality. Therefore, the solids volume fractions in the researches were usually limited to 1% (Unadkat et al., 2009; Montante et al., 2012; Guiraud et al., 1997). In order to solve this problem, the refractive index matching (RIM) method was proposed and applied in the stirred tanks that carry out solid-liquid mixing processes (Li et al., 2018; Virdung and Rasmuson, 2007a, 2007b; Gabriele et al., 2011; Micheletti and Yianneskis, 2004). In most experimental studies on solid-liquid flow, the spatial resolution of the optical techniques is such that flow around individual particles cannot be resolved. In previous work (Li et al., 2018) we performed refractive index matched PIV experiments with a resolution of approximately one velocity vector per millimeter in a turbulent solid-liquid flow system with 8 mm diameter particles. This combination of resolution and particle size allowed us to study the flow around individual particles in a dense suspension (tank-averaged solids volume fractions up to 8%) (Li et al., 2018). In the present paper a similar experimental approach is taken, now for a flow system in the transitional regime. In addition, we will present results of particle-resolved numerical simulations of the same systems as studied experimentally so as to compare simulation results with the highly resolved experimental data.

Numerical simulations of solid-liquid two-phase systems can be divided in Eulerian-Lagrangian (E-L) and Eulerian-Eulerian. In the latter, liquid and solids phase are treated as (interpenetrating) continua; in the former, discrete particles are tracked through a continuous liquid phase. In this paper only the E-L approach will be considered. Generally, direct numerical simulation (DNS) or large-eddy simulation (LES) are favorable choices to deal with the continuous phase compared to an approach based on the Reynolds-averaged Navier-Stokes (RANS) equations when studying the turbulent characteristics in a stirred tank by an E-L approach. This is because the role of stochastic particle tracking models to account for the effects of turbulence on particle motion is more important in RANS than it is in LES, and no stochastic model is needed in a DNS. In applications dealing with dilute solid-liquid systems the effects of the finite size of the particles as well as particle-particle interactions have often been ignored (Derksen, 2003). By applying volume-averaged Navier-Stokes equations, collision and lubrication force models as well as drag correlations that take into account the local solids volume fraction, more recent work does incorporate finite size effects and is therefore able to realistically deal with dense suspensions (Derksen, 2018).

Since in many cases contacting liquid and solid is an important goal of agitated solid-liquid systems, the phenomena that occur at the particle scale are at least as important as overall characteristics such as power consumption and mixing times. In

computational work this translates in a trend towards resolving flow and scalar transport at the length scales of the particles (Derksen, 2012, 2014a). This trend is facilitated by the increasing availability of computational resources as well as developments in numerical methods. Nowadays Eulerian-Lagrangian simulations are feasible with millions of point particles being tracked through the liquid phase (Derksen, 2006, 2009, 2018), thereby revealing extensive detail of liquid and solids dynamics as well as the possibility to record the history of exposure to flows and scalar concentrations of individual particles (Derksen, 2014b). In simulations with even finer resolution, the flow around individual particles is resolved. This largely eliminates the need for empirical input (e.g. for the drag force, or mass transfer coefficients) in the simulations. In such particle-resolved simulations the grids on which the liquid flows are solved typically have spacings that are one order of magnitude smaller than the particle size and thus are able to explicitly impose no-slip and non-penetration (for mass transfer) conditions at the actual solid-liquid interface (Derksen, 2012, 2014a, 2014b).

As for virtually all simulations, guidance and validation from experimental work is vital. Given the high resolution reached in simulations, we seek comparable resolution in experiments: we are looking for experimentally resolving the flows around individual particles suspended in an agitated tank in the transitional flow regime under moderate to high solids loading conditions. This has been achieved by an experimental setup with refractive index matching of solids and liquid. In this setup PIV is applied with a spatial resolution much finer than the size of the spherical particles.

The aim of this article is firstly to perform highly resolved experiments on the liquid flow field including the flow around the particles thereby investigating solid-liquid interactions at the particle scale in a dense, agitated suspension. In the second place, the process of solid-liquid suspension is mimicked by using particle-resolved simulations based on the lattice-Boltzmann (LB) method under the same operating conditions as in the experiments. The presence of particles influences the flow behavior in the mixing tank. This we investigate by characterizing the system in terms of averages of statistical quantities such as velocity, velocity fluctuation levels, and local solids volume fraction. The third aim of the paper is to assess to what extent particles influence liquid flow properties and how simulations are able to represent these effects in the light of the highly resolved experimental data. In the fourth place, the research as described in this paper has generated a unique set of experimental data that is available for validation of numerical approaches different from the one we have described here.

This paper is organized as follows: in the next section, the experimental setup is discussed, including the flow system, properties of the solids and liquid, PIV system and image processing. Then, the LB-based numerical approach is briefly summarized. Subsequently, in the “Results and Discussion” section, we firstly present the evolution of the solid-liquid

suspension process in the simulations and then compare the simulated results with the experimental data in both instantaneous and statistically averaged sense. The last section provides the conclusions.

2. Experimental setup

2.1 Flow system

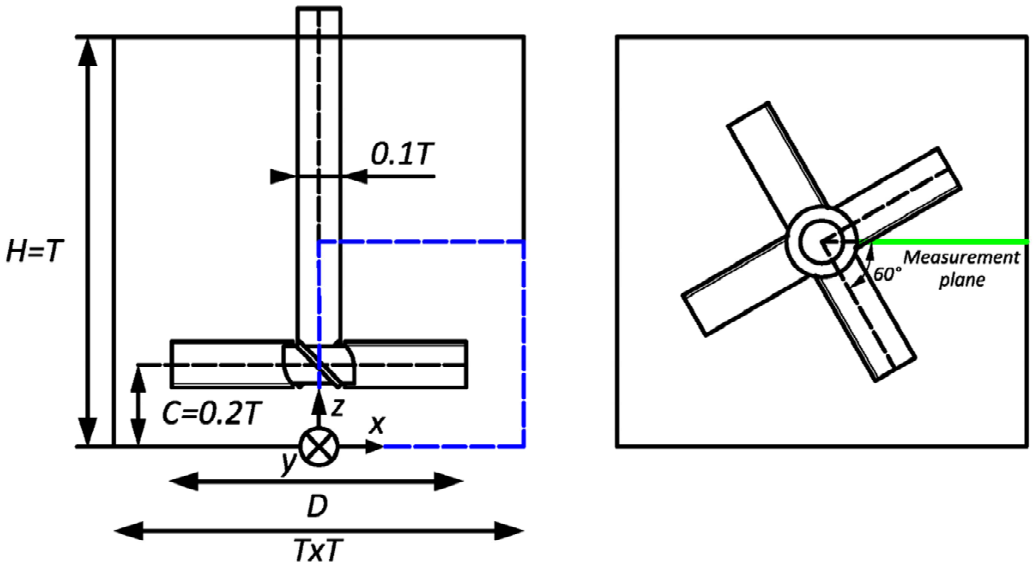

Fig. 1. Stirred tank geometry, coordinate system and the measurement plane. Gravity points in the negative *z*-direction. The impeller angle equals to 60° with respect to the measurement plane and the impeller rotates clockwise in the right panel thereby pumping liquid in the downward direction.

The stirred tank has height h = 300 mm and a square bottom whose side length (T) is 220 mm. The tank is made of transparent tempered glass and a PMMA lid was set at the vertical position $H = T$. This is used to avoid air entrainment and at the same time to provide a no-slip boundary condition at the liquid surface, in accordance with the boundary condition in the numerical simulations. The impeller is a 45° pitched-blade turbine (diameter D = 158 mm, four blades) that operates in the down-pumping configuration. The off-bottom clearance (C) is 44 mm ($C = T/5$). The measurement plane in the experiments is marked as the blue frame in the left panel in Figure 1, which was between $0 < z/H < 0.5$ and $0 < x/T < 0.5$. The impeller angle (θ) between the measurement plane and the impeller blade was fixed to 60^{o} as shown in the right panel in Figure 1.

2.2 Experimental materials and refractive index matching method

Table 1

Properties of the liquid and solids at 21°C.

	sucrose and sodium chloride aqueous solution	silica glass spheres
Density (kg m^{-3})	1357	2210
Dynamic viscosity (Pa·s)	0.1904	
Refractive index	1.4601	1.4600

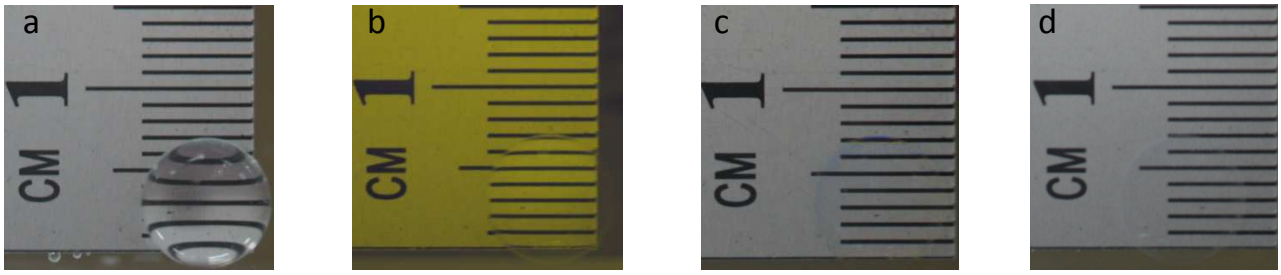

Fig. 2. Images of a silica glass sphere (refractive index n = 1.4600) immersed in (a) deionized water (n = 1.3322); (b) olive oil (n = 1.4672); (c) phenyl silicone oil (n = 1.4610); (d) sucrose and sodium chloride aqueous solution (n = 1.4601) at T = 21°C.

The same silica glass spheres (average diameter d_p = 8 mm with a standard deviation of 0.2 mm) as used in our previous research (Li et al., 2018) are selected as the disperse phase in the current study. A sucrose and sodium chloride aqueous solution (sucrose: sodium chloride: deionized water = 84 : 10 : 50 by weight) was made and used as the continuous phase to match the refractive index (RI) n of the disperse phase. This way it is possible to measure the liquid velocities in the presence of particles up to a solids volume fraction Φ = 8%. The specific properties of both the continuous phase and the disperse phase are listed in Table 1. Figure 2 illustrates that the optical distortion becomes obvious when the RI difference reaches around 0.007 (compare Figure 2b and Figure 2d). The distortion nearly disappears (at least by naked eye) when the RI difference becomes less than 0.001 (compare Figure 2c and Figure 2d). A change of temperatures will affect the RI value as well as the viscosity of the liquid. Therefore, in order to ensure the accuracy of the experiments, the temperature was controlled and kept at 21 ± 0.5 °C. For the liquid used in the current experiments, the RI value and the dynamic viscosity decrease by 0.00023 and 0.0087 Pa·s (4%) respectively with a rise in temperature of 1 °C.

2.3 Operating conditions

This paper mainly focuses on how the presence of solids affects the liquid flow field in the mixing tank. We have generated five PIV experimental data sets with different tank-averaged solids volume fractions: 0%, 1%, 3%, 5% and 8%. The impeller speed and the angle between the impeller and the measurement plane have been fixed to N = 450 rpm = 7.5 rev/s and $\theta = 60^{o}$ respectively. With the liquid kinematic viscosity $\nu = \mu/\rho = 1.4 \cdot 10^{-4}$ m^2/s as can be derived from Table 1, the impeller-based Reynolds number is $Re \equiv \frac{ND^2}{\nu} = 1334$ which indicates that the flow is in the transitional regime (Paul et al., 2004). The just-suspended impeller speed correlation due to Zwietering (1958) reads

$$N_{js} = s \frac{(d)^{0.2} \nu^{0.1} (100\phi \rho_s/\rho)^{0.13}}{D^{0.85}} \left(\frac{g\Delta\rho}{\rho} \right)^{0.45} \quad (1)$$

As a coarse estimate, if we set the dimensionless parameter s = 5 and Φ = 8% in the equation above, then N_{js} = 11.9 rev/s. The impeller speed in the current study thus is lower than N_{js}, at least for Φ = 8%, which implies a situation with not fully suspended solids. If we take the inverse of the blade-passage frequency – $1/(4N)$ – as the time scale of the flow then the Stokes number is $St \equiv \frac{2}{9} \frac{\rho_s}{\rho} \frac{d^2 4N}{\nu}$ = 4.95. The Archimedes number is $Ar \equiv \frac{g\Delta\rho d^3}{\rho\nu^2}$ = 160 and the Shields number is $\theta \equiv \frac{\rho N^2 D^2}{gd\Delta\rho}$ = 28.4 with g the gravitational acceleration and $\Delta\rho = \rho_s - \rho$ the density difference between the solids and the liquid.

2.4 PIV experiments

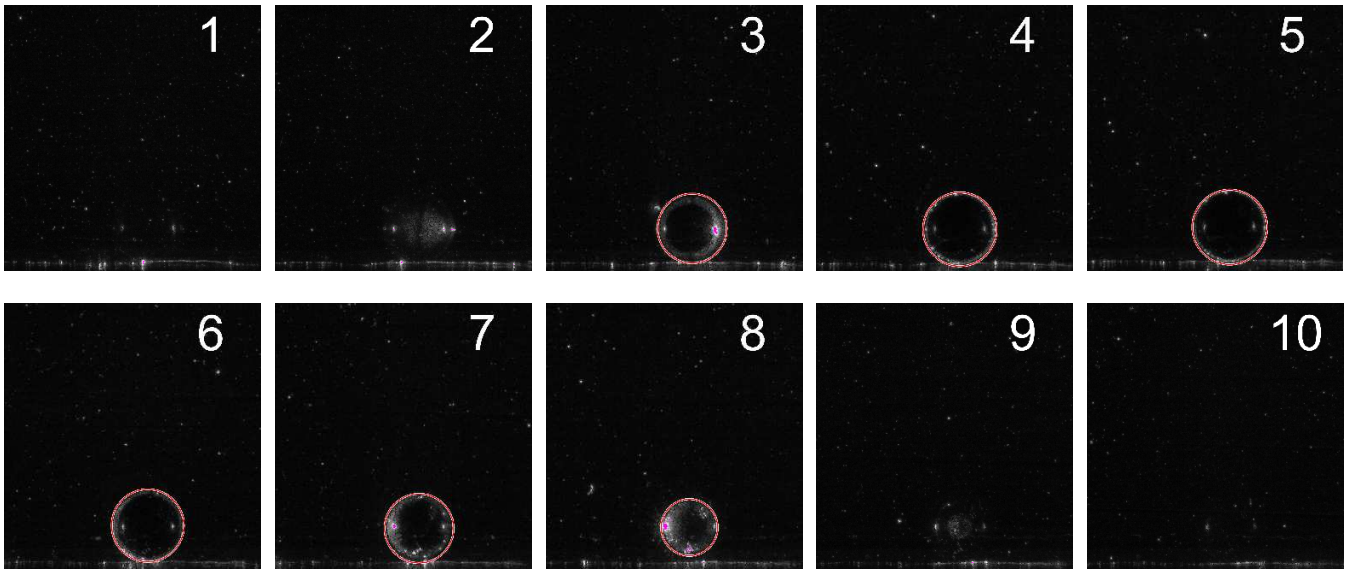

Fig. 3. Camera frames shot with the PIV system with one single silica glass sphere laying still on the bottom of the tank. From image to image, the laser sheet has been moved by 1 mm in the direction normal to the field of view.

The same 2D-PIV system (TSI) as in Li et al. (2018) was used in the current study. It consists of a 532 nm 200mJ Nd:YAG dual pulse laser, a 4008×2672 pixels charge coupled device camera, a synchronizer, an encoder and a PC loaded with TSI INSIGHT 3G software. The tracer particles used in the experiments were hollow glass beads with diameters of about 8-12 µm and density of 1500 kg/m^3. If we base the Stokes number of the tracer particles on the Kolmogorov time scale and estimate the latter as $\tau = Re^{-1/2}/4N$ then $St = Re^{1/2}\frac{2}{9}\frac{\rho_t}{\rho}\frac{d_t^2 4N}{\nu} \approx 2\cdot 10^{-4}$ (with d_t the tracer particle diameter and ρ_t their density). This shows that the tracer particles are able to adequately respond to fluctuations at the Kolmogorov time scale.

In the PIV experiments, the size of the interrogation windows was 48X48 pixels with 50% overlap. The resolution of the images was 41.60 µm/pixel which led to a velocity vector resolution of 1.0 mm. Thus, there are eight vectors per particle diameter, which means the flow fields around the particles are well resolved. The INSIGHT 3G software that is used to process and analyze the PIV data goes through the following stages: first, a Fast Fourier Transform algorithm is applied to carry out the cross-correlation processing; second, the Nyquist Grid combined with ZeroPad Mask method was adopted to interrogate the cross-correlation fields; third, the Gaussian subpixel estimator was applied to mitigate peak-locking effects (Christensen, 2004).

The PIV images have also been analyzed with the purpose of detecting the solids spheres in order to determine spatial distributions of the solids volume fraction. The circular boundaries of the spheres in the raw PIV images have been detected by the same Matlab code used in our previous investigation (Li et al., 2018). The principal steps in this code are the adjustment of

the image intensity and the Circular Hough Transform (CHT) algorithm. The Matlab function *imadjust* was used to increase the contrast of the image after transforming the raw RGB PIV images into gray images. The Matlab function *imfindcircles* (MathWorks Inc, 2016) was used to perform the CHT to find the circles in the images. The main input parameters in the latter function were set as follows: 'Bright' and 'PhaseCode' were chosen for the *Object polarity* and the *Computation method*, respectively (Atherton and Kerbyson, 1999). The *Sensitivity factor* was set to 0.93, and the *Edge gradient threshold* to 0.01. More details about how these parameters were determined can be found in Li et al. (2018). This detection process is very important because this makes it possible not only to determine where the spheres are in the stirred tank but also to remove the unphysical liquid velocity vectors inside the spheres. However, it should be noted that the particle velocities cannot be measured in the current experimental setup. One reason is that the PIV capture frequency is too low (1 Hz) so that the impeller has rotated about eight revolutions in the one-second period between two successive PIV captures. Another reason is that the time interval between the two frames of one PIV capture is too short (60 μs) to reliably measure the particle's displacement and so obtain an accurate particle velocity estimate (Feng et al., 2011).

The thickness of the laser sheet in our PIV system is about 1 mm. In order to see how one particle was illuminated by the laser sheet, was registered by the camera, and how the image of the particle was processed, we performed a simple experiment. We placed one silica glass sphere with diameter of 8 mm on the bottom of the tank and kept it static. We moved the laser sheet carefully so that it just illuminated the edge of the sphere (see image 1 in Figure 3). Then we moved the laser sheet along the particle diameter with steps of one millimeter and captured the particle (see images 2-9 in Figure 3) until the laser sheet did not touch the sphere anymore (see image 10 in Figure 3). The images in Figures 3 clearly show the outline of the particle when it was illuminated at different positions relative to the sheet and confirm the one-millimeter thickness of the laser sheet. The image sequence is not perfectly symmetric; there are some differences between images 3 and 8 as well as images 4 and 7 in Figure 3. The particle in images 3 to 8 in Figure 3 can be accurately detected, as indicated by the red circles in Figure 3. In calculating the simulated solids volume fraction, we also took into account a plane with thickness of 1 mm. Any particle in contact with the one-millimeter plane was included in calculating the local solids volume fraction. In the experiment, the particle cannot be detected when it is only illuminated by the very edge of the laser sheet, as shown in the images 2 and 9 in Figure 3. Such particle positions, however, are considered when processing the simulation results so that in this respect the experimental solids volume fraction might be slightly underestimated.

2.5 Flow field analysis

Five different series of PIV experiments were performed having tank-averaged solids volume fractions (Φ) of 0%, 1%, 3%, 5% and 8% and a fixed impeller angle of $\theta = 60^{o}$. In each series, 500 image pairs were captured and used to analyze and calculate the distribution of averaged solids volume fraction and the averaged liquid velocity fields. As demonstrated in our previous investigation (Li et al., 2018), 500 realizations are sufficient to achieve statistically converged averages. For the latter, the radial, tangential, and axial impeller-angle-resolved average velocities of the liquid were defined as $\bar{U}_\theta, \bar{V}_\theta, \bar{W}_\theta$, respectively with θ indicating the averages are taken at a fixed impeller angle (60^{o} in the current study). The root-mean-square (rms) velocities are used to characterize the fluctuation levels of the liquid velocities, for example, the radial rms velocity is defined as $U'_\theta = \sqrt{\overline{\left(U_\theta - \bar{U}_\theta\right)^2}}$. The turbulent kinetic energy (TKE) *k* of the liquid is defined as: $k = \frac{1}{2}\left(U'^2_\theta + V'^2_\theta + W'^2_\theta\right)$. Since we did not measure the tangential velocities in the 2D-PIV experiments, the tangential rms velocity has been approximated as $V'^2_\theta = \frac{1}{2}\left(U'^2_\theta + W'^2_\theta\right)$ based on a local pseudo-isotropic assumption (Gabriele et al., 2011; Liu et al., 2010). Therefore, the TKE has been approximated as $k \approx \frac{3}{4}\left(U'^2_\theta + W'^2_\theta\right)$ (Khan et al., 2006). The same procedure was applied to the simulations in order to have a fair comparison between the experimental date and simulated results. When presenting results in this paper, all velocities were normalized by the impeller tip speed v_{tip}, and the TKE was normalized by v^2_{tip}.

3. Numerical simulations

The process of solid-liquid suspension was also investigated by numerical simulations. The simulation procedure was the same as that used in Derksen (2012). In the simulations, all the geometrical parameters, physical properties and operation conditions were set the same as those in the PIV experiments by matching the dimensionless numbers of the experiments.

The LB method (Chen and Doolen, 1989; Succi, 2001) based on the scheme proposed by Somers and Eggels (Somers, 1993; Eggels and Somers, 1995) was used to solve the liquid flow field. The method uses a uniform, cubic grid. The grid spacing Δ and the time step Δt were used to represent the lattice units in space and time respectively. The side length of the stirred tank was represented by 264 grid spacings (T = 264Δ), therefore the impeller diameter D = 189.6Δ and the diameter of the spherical particles was d_p = 9.6Δ. The requirement for the grid resolution is estimated by relating the Kolmogorov length scale (η) to the

macroscopic length scale - for which we take the impeller diameter D (an intermediate between tank size and blade dimensions) (Derksen, 2003, 2012) - via the Reynolds number: $\eta = D \cdot Re^{-3/4} \approx 0.86\Delta$ (Tennekes and Lumley, 1973), with Re = 1334. The resolution of our simulations thus satisfies the typical criterion for carrying out a DNS: $\Delta \leq \pi\eta$ (Moin and Mahesh, 1998; Eswaran and Pope, 1988).

In order to simulate incompressible flow, liquid velocities need to stay well below the speed of sound of the LB scheme, in which the speed of sound is of order one in lattice units. This is achieved by limiting the impeller tip speed – which is a good measure for the highest liquid speed in the tank – to 0.1 in lattice units which is realized by setting the impeller to make one revolution in 6120 time steps. The kinematic viscosity was set as $\nu = 0.0044$ (in lattice units) to match the Reynolds number in the experiments.

In terms of the boundary conditions, the no-slip boundary condition was applied to the tank walls (bottom, top and side walls) by means of the half-way bounce-back rule (Succi, 2001). The immersed boundary method (Derksen and Van den Akker, 1999; Ten Cate et al., 2002; Goldstein et al., 1993) was adopted to impose the no-slip condition at the surfaces of the impeller and the particles.

With respect to collisions, a hard-sphere collision algorithm according to two-parameters model (restitution coefficient e and friction coefficient μ) (Yamamoto et al., 2001) was used to perform the collisions among the spheres as well as the collisions between the spheres and the tank wall. In solid-liquid systems, the energy dissipation of particles largely happens in the liquid, not so much during collisions between particles. Therefore, the restitution coefficient is not a critical parameter when studying the overall suspension behaviour (Derksen and Sundaresan, 2007). The restitution coefficient was set to $e = 1$ in the whole study. For the friction coefficient, a previous numerical study of erosion of granular beds (Derksen, 2011) shows that a zero or a nonzero friction coefficient will affect the results significantly. However, the precise nonzero value has only weak impact on the behaviour of the flow system. With $\mu = 0.1$, the simulations could reproduce the experimental data on incipient bed motion correctly, therefore the same μ was used in this work. For the collisions between the spherical particles and the impeller, a soft-sphere collision model was adopted, in which a repulsive force is exerted on a particle when its volume overlaps that of the impeller. In order to ensure the stability of the numerical simulations and at the same time limit the maximum overlapping volume of a particle with the impeller to approximately 0.5% of the particle volume, the collision time was set to $10\Delta t$; during this time the impeller rotates approximately 0.6°.

For close-range hydrodynamic interaction between the particles we apply lubrication force modeling where we limit ourselves to the radial lubrication force. Based on the creeping flow assumption for the flow in the space between two spherical surfaces undergoing relative motion (Kim and Karrila, 1991), the radial lubrication force between two spheres *i* and *j* is:

$$\mathbf{F}_{\mathbf{lub}} = 6\pi\rho\nu \frac{a_i^2 a_j^2}{(a_i + a_j)^2} \frac{1}{s} \left(\mathbf{n} \cdot \Delta\mathbf{u}_{\mathbf{ij}}\right) \mathbf{n} \tag{1}$$

In equation (1), a_i and a_j are the radii of sphere *i* and *j*, respectively. *s* is the smallest distance between the surfaces of these two spheres, which is $s = \left|\mathbf{x}_{\mathbf{pj}} - \mathbf{x}_{\mathbf{pi}}\right| - \left(a_i + a_j\right)$ with $\mathbf{x}_{\mathbf{pi}}$ and $\mathbf{x}_{\mathbf{pj}}$ the sphere center locations. The vector **n** is the unit vector pointing from $\mathbf{x}_{\mathbf{pi}}$ to $\mathbf{x}_{\mathbf{pj}}$ and $\Delta\mathbf{u}_{\mathbf{ij}} = \mathbf{u}_{\mathbf{pj}} - \mathbf{u}_{\mathbf{pi}}$ is the relative velocity between sphere *i* and *j*. When applying equation (1) to the case between a sphere and the tank, a_j is then set to infinite and $\mathbf{u}_{\mathbf{pj}}$ is set to **0**.

Equation 1 has been adapted in two ways: lubrication only becomes active when the distance between two sphere surfaces gets smaller than the grid spacing, and the lubrication force saturates when the surfaces are so close that surface roughness would limit the lubrication force (Nguyen and Ladd, 2002):

$$\begin{aligned}
&\mathbf{F}_{\mathbf{lub}} = 6\pi\rho\nu \frac{a_i^2 a_j^2}{(a_i + a_j)^2} \left(\frac{1}{s_1} - \frac{1}{s_0}\right) \left(\mathbf{n} \cdot \Delta\mathbf{u}_{\mathbf{ij}}\right) \mathbf{n} && s \le s_1 \\
&\mathbf{F}_{\mathbf{lub}} = 6\pi\rho\nu \frac{a_i^2 a_j^2}{(a_i + a_j)^2} \left(\frac{1}{s} - \frac{1}{s_0}\right) \left(\mathbf{n} \cdot \Delta\mathbf{u}_{\mathbf{ij}}\right) \mathbf{n} && s_1 < s < s_0 \\
&\mathbf{F}_{\mathbf{lub}} = \mathbf{0} && s \ge s_0
\end{aligned} \tag{2}$$

In equation(2), s_0 is the upper limit of the distance above which the lubrication forces is switched off; s_1 is the lower limit of the distance below which the lubrication forces get saturated. The settings for s_0 and s_1 were $s_0 = 0.1 d_p$ and $s_1 = 10^{-4} d_p$. It should be noted that the tangential lubrication forces and torques were neglected because they are much weaker compared to the force in the radial direction.

4. Results and discussion

4.1 Impression of simulated solid-liquid suspension

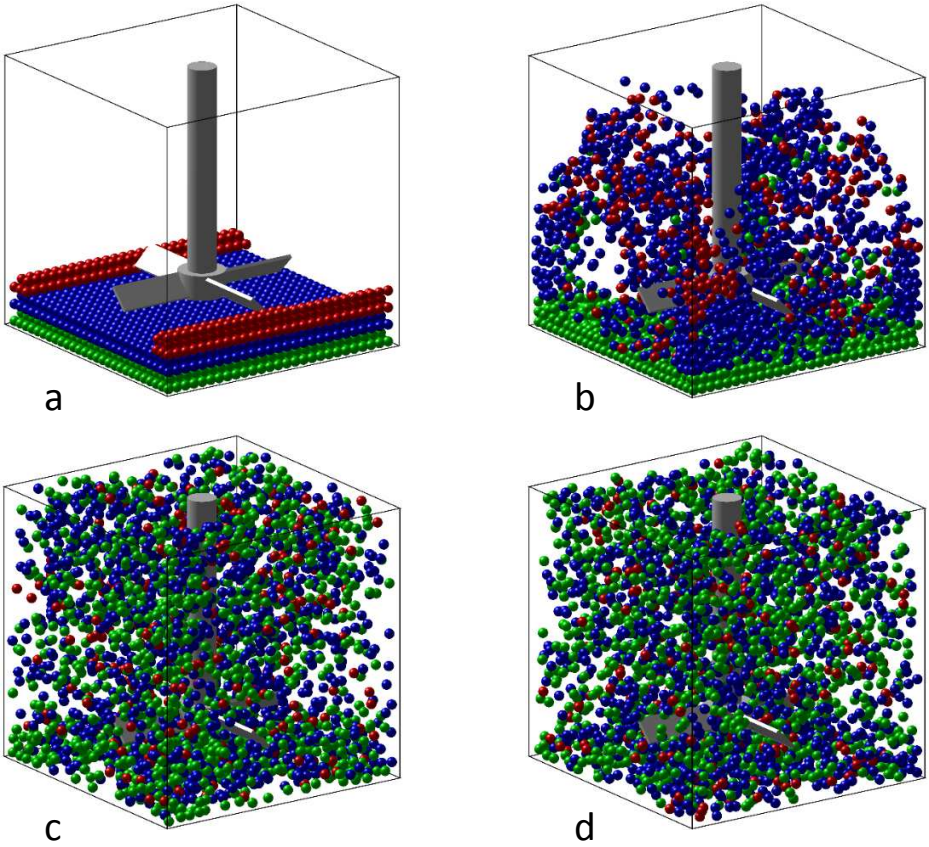

Fig. 4. Instantaneous realizations of particle distributions in the stirred tank during the suspension process with tank-averaged solids volume fraction Φ = 8% at four different moments: (a) initial state; (b) after three impeller revolutions; (c) after twenty impeller revolutions; (d) after fifty impeller revolutions.

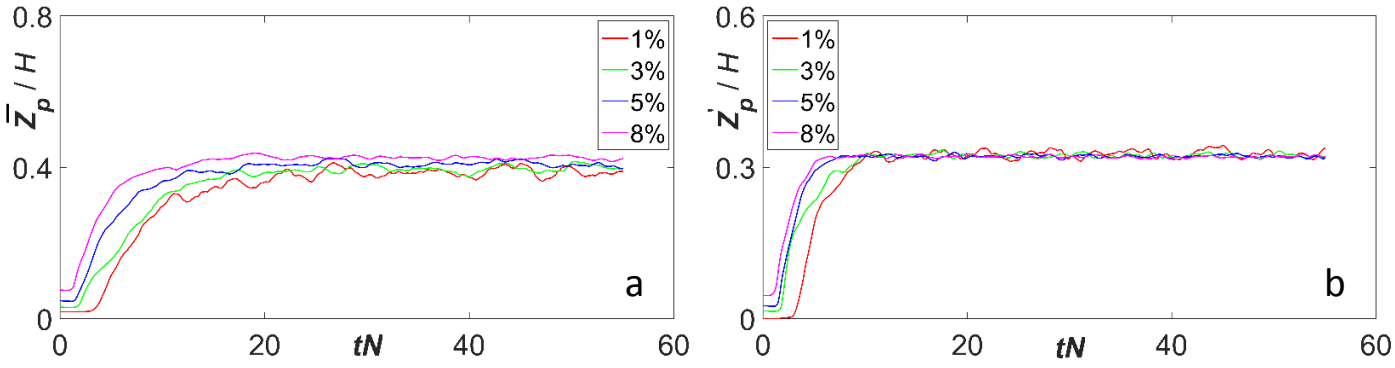

Fig. 5. Time series of (a) averaged vertical locations of all particles; (b) rms values of the vertical particle locations. Overall solids volume fraction as indicated.

The process of solids suspension with Φ = 8% in the numerical simulation is shown as Figure 4. The particles were arranged in a regular pattern and closely spaced on the bottom of the tank. Different colors (red, blue, green) indicate different layers of particles from top to bottom (see Figure 4(a)). After three impeller revolutions, nearly all red and blue particles are suspended while most green particles still rest on the bottom, with the exception of some green particles in the corners. Figure 4(c) and Figure 4(d) show that most particles are suspended and well mixed throughout the tank volume after twenty impeller revolutions.

The average and rms values of the vertical particle locations in the tank are used to determine after how many impeller revolutions the solid-liquid system reaches a dynamic steady state. The average value is defined as $\overline{z_p} = \frac{1}{M}\sum_{i=1}^{M} z_{pi}$ and the rms value is defined as $z_p^{'} = \sqrt{\frac{1}{M}\sum_{i=1}^{M}\left(z_{pi} - \overline{z_p}\right)^2}$ with M the number of the particles and z_{pi} the vertical location of particle i. From Figure 5, we can see that both the average and rms values of the vertical particle locations fluctuate slightly after reaching steady state. In steady state, the average vertical location increases slightly with increasing overall solids volume fraction; the rms values are insensitive to the change of solids volume fraction. The results in Fig. 5 indicate that the simulations have reached a dynamic steady state after twenty impeller revolutions. Therefore, all the simulated data used to calculate statistical flow quantities are based on data obtained after twenty impeller revolutions. As in the experiments, we base our simulated statistics on 500 independent flow realizations.

4.2 Comparisons between numerical and experimental results

4.2.1 Instantaneous particle distributions and instantaneous flow realizations

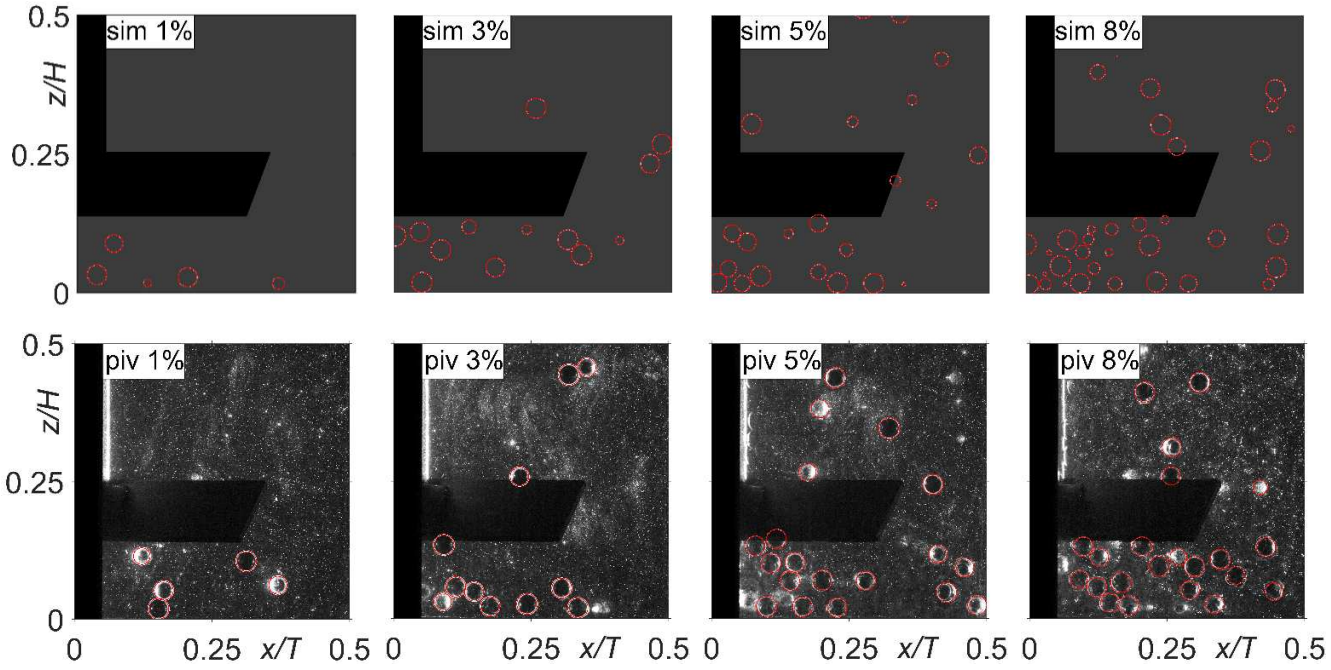

Fig. 6. Instantaneous particle distributions in the vertical middle plane of the stirred tank with tank-averaged solids volume fraction Φ = 1%, 3%, 5% and 8% at impeller angle $\theta = 60^{o}$ from left to right. The simulated results are on the top row and the experimental results are on the bottom row.

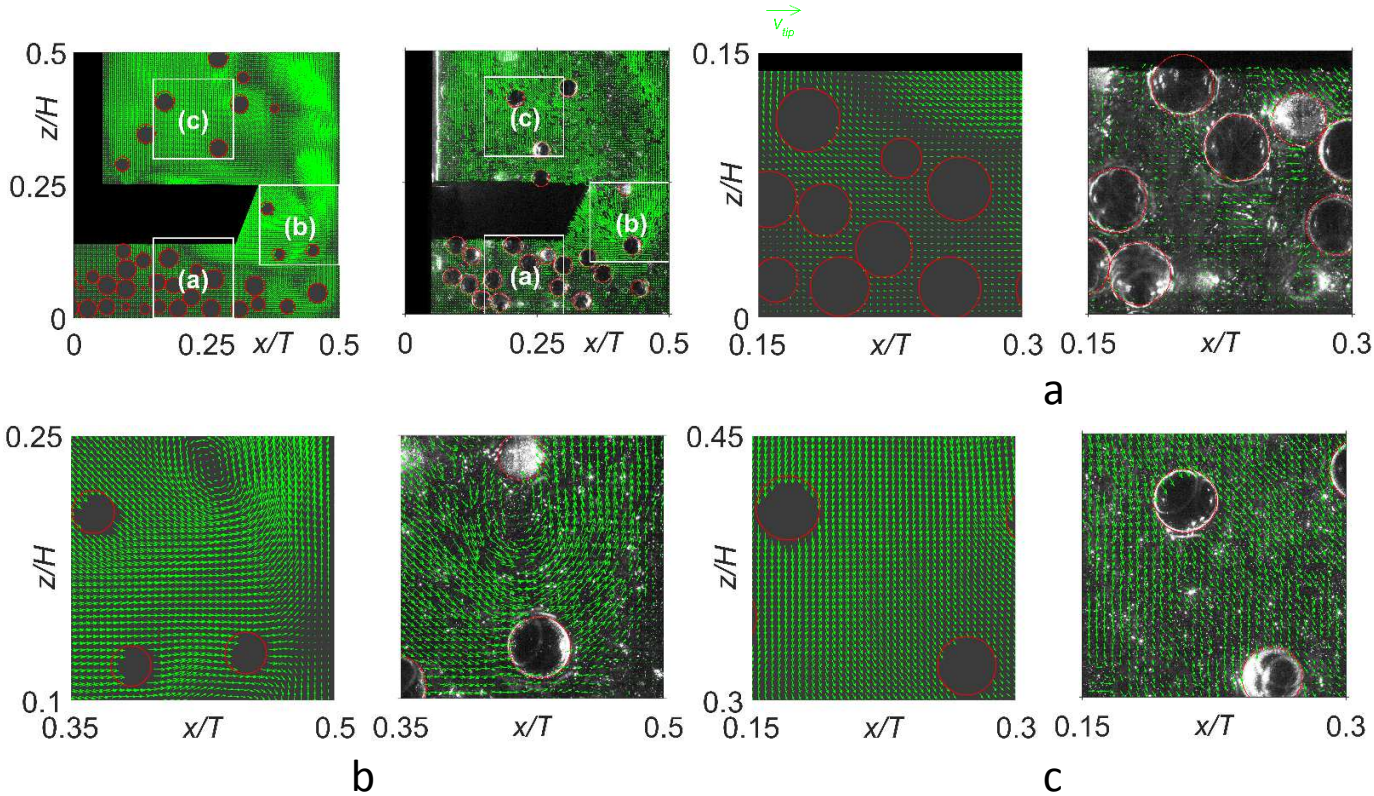

Fig. 7. Comparisons of instantaneous liquid velocity field at different locations in the stirred tank with Φ = 8% at impeller angle $\theta = 60^{o}$ between the simulated results (on the left panel of each sub-figure) and the experimental results (on the right panel of each sub-figure). The region of each sub-figure (a) (b) (c) in the stirred tank are marked in the sub-figure at top left and the reference vector at top applies to all sub-figures.

The grid spacing in the simulations is comparable to the laser sheet thickness (Δ = 0.83 mm versus a sheet thickness of 1 mm). In comparing simulation and PIV result we thus present simulation data in one, vertical grid plane through the center of the tank. The circumference of particles shown in the simulated result is their cross section with the middle of this plane. The circles shown in the PIV frames are the ones detected by the Matlab routine.

First we show instantaneous particle distributions and instantaneous liquid velocity fields in the middle plane. Figure 6 compares the instantaneous particle distributions in the simulations with those from the experiments for different tank-averaged solids volume fractions at impeller angle $\theta = 60^o$. Experiments as well as simulations show that particles preferentially concentrate underneath the impeller and that the particles are only partially suspended as was expected based on the just-suspended impeller speed (N_{js}) estimates. Figure 7 shows the instantaneous liquid flow fields for the case with Φ = 8% at impeller angle $\theta = 60^o$. As we can see from Figure 7, the flow fields around the particles are well resolved in the experiment as well as in the simulation. The flow close to the bottom (zone a in Figure 7) is very weak due to the presence of many particles there. The other zones have stronger flow, including the impeller discharge stream in zone b. The frames in Figure 7 qualitatively show the way the particles hinder the liquid flow, a phenomenon that will be discussed below in a more quantitative sense. The velocity vector fields from the simulations are smoother than those form the PIV experiments and therefore one might expect (turbulent) fluctuations to be weaker in the simulations. Velocity fluctuation levels and how they compare between experiment and simulation are further investigated below when statistical velocity properties are analyzed.

4.2.2 Averaged solids volume fraction

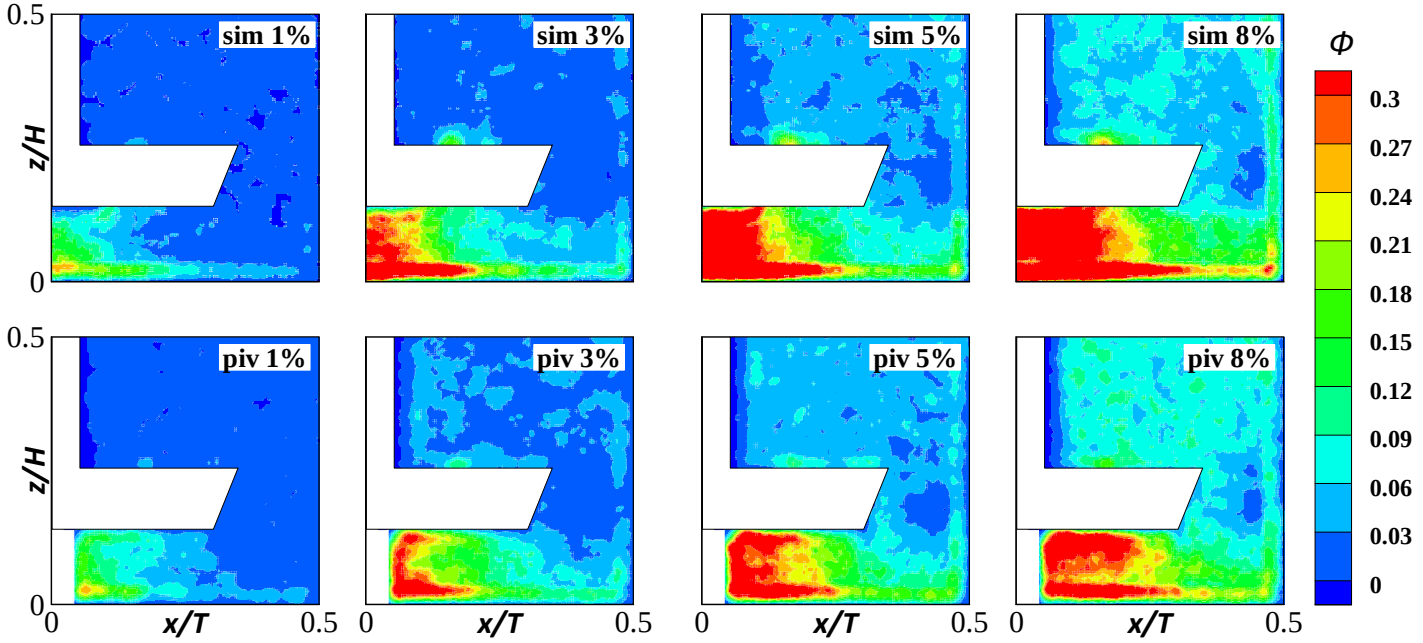

Fig. 8. Averaged solids volume fraction contours with different tank-averaged particle volumetric concentrations: 1%; 3%; 5% and 8% at impeller angle θ = 60° from the left to right. The simulated results are on the top row and the experimental results are on the bottom row.

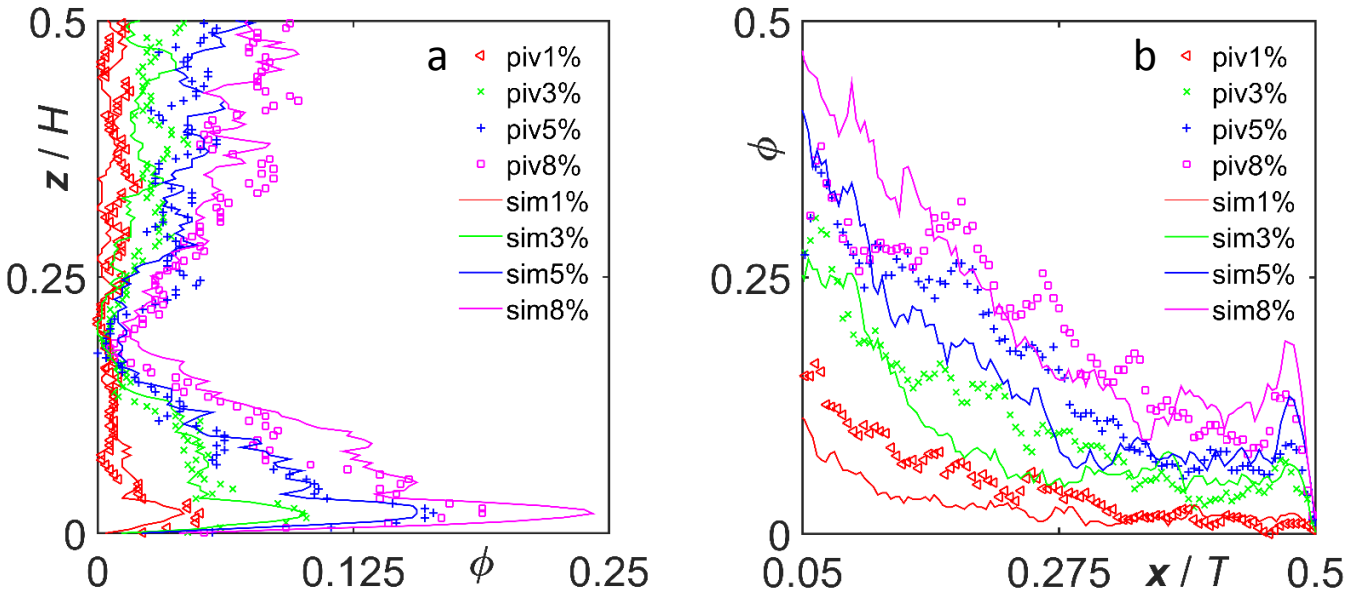

Fig. 9. Profiles of averaged solids volume fraction for different particle volumetric concentrations with impeller angle θ = 60° at (a) *x/T* = 0.45; (b) *z/H* = 0.08.

Figure 8 shows the averaged solids volume fractions in the measurement plane in the stirred tank (see the blue frame in Figure 1) with impeller angle θ = 60° for four levels of tank-averaged solids volume fraction. In the simulations, the solids volume fraction in the field of view has been determined by calculating the surface fraction of the cross section of the

spherical particles with a 1 mm thick (the thickness of the laser sheet) vertical layer through the center of the tank. In the experiments, it is the surface fraction of the particles detected by the circle-detection Matlab routine that was explained above. From Figure 8, we can see that both the experimental and simulated solids concentrations are highest underneath the impeller, which is indicative of this being a case with partially suspended solids. The solids concentrations are also relatively high in the corners of the tank and near the tank walls. The swirling flow induced by the impeller generates centrifugal forces on the particles (that have a density larger than that of the fluid) which pushes the particles against the side walls. Particles getting briefly stuck in the corners of the tank add to increased levels of solids concentration there. The residence time of particles in the impeller stream – on the other hand – is very short thus leading to relatively low levels of solids concentration in this region.

Profiles of the solids volume fractions are shown in Figures 9. The vertical profile at x/T = 0.45 (close to the side wall) in Figure 9(a) shows that the peak levels close to the bottom are well predicted by the simulations up to Φ = 5%. For Φ = 8% the simulation somewhat overestimates the peak near the bottom. The low solids region at the level of the impeller is consistent between experiments and simulations. The horizontal profile close to the bottom (Figure 9(b)) show the accumulation of solids underneath the impeller. The extent to which this happens is represented well by the simulations. Even subtle details such as a modest peak near the side wall in the horizontal profile as seen in the experiment are reproduced by the simulation.

4.2.3 Mean velocities and velocity fluctuations of the liquid

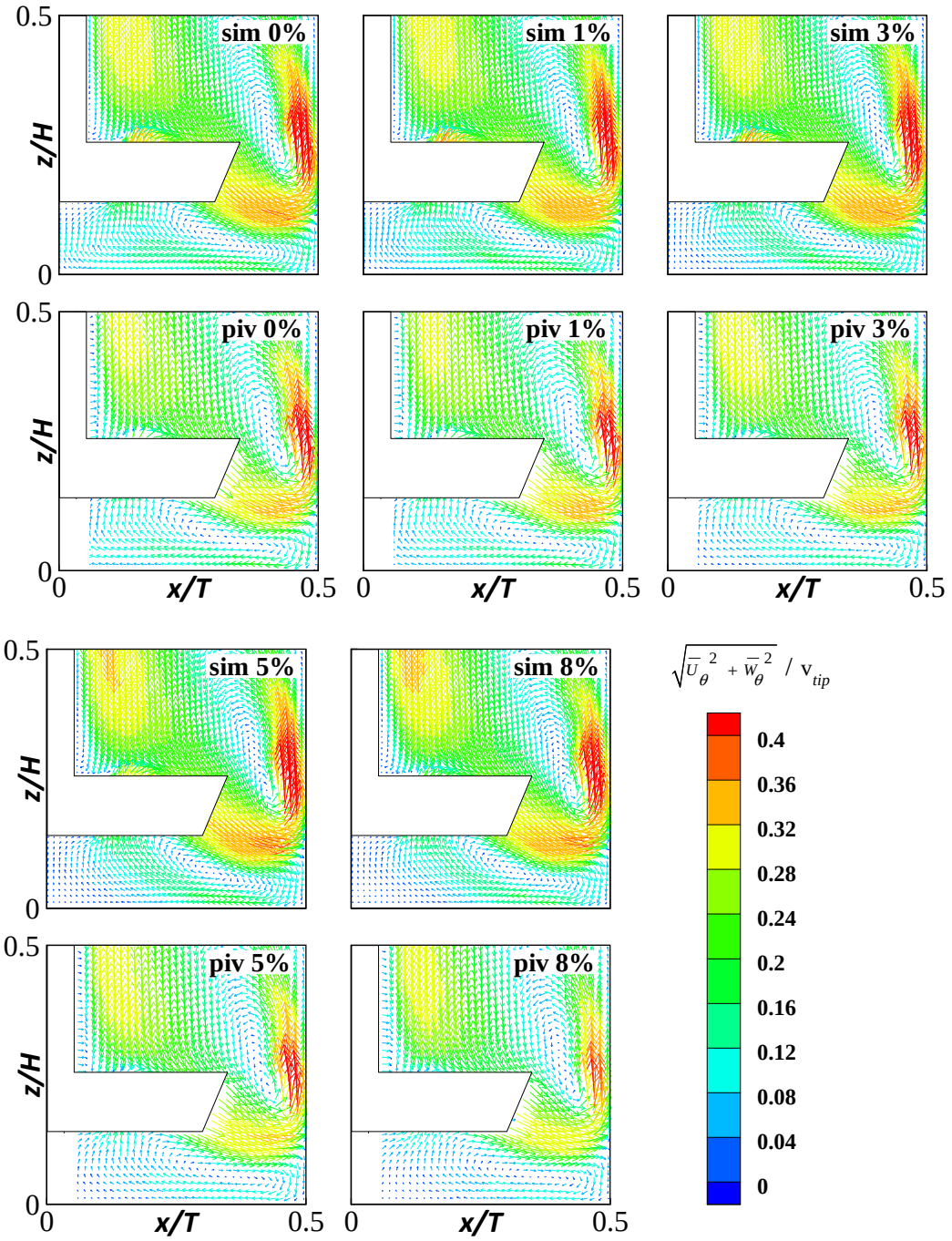

Fig. 10. Normalized liquid averaged velocity field for different solids volume fractions: 0%, 1%, 3%, 5% and 8% at impeller angle θ = 60°. The resolutions of both the experiments and the simulations are three times as high in each direction as the density of the velocity vectors in the figure.

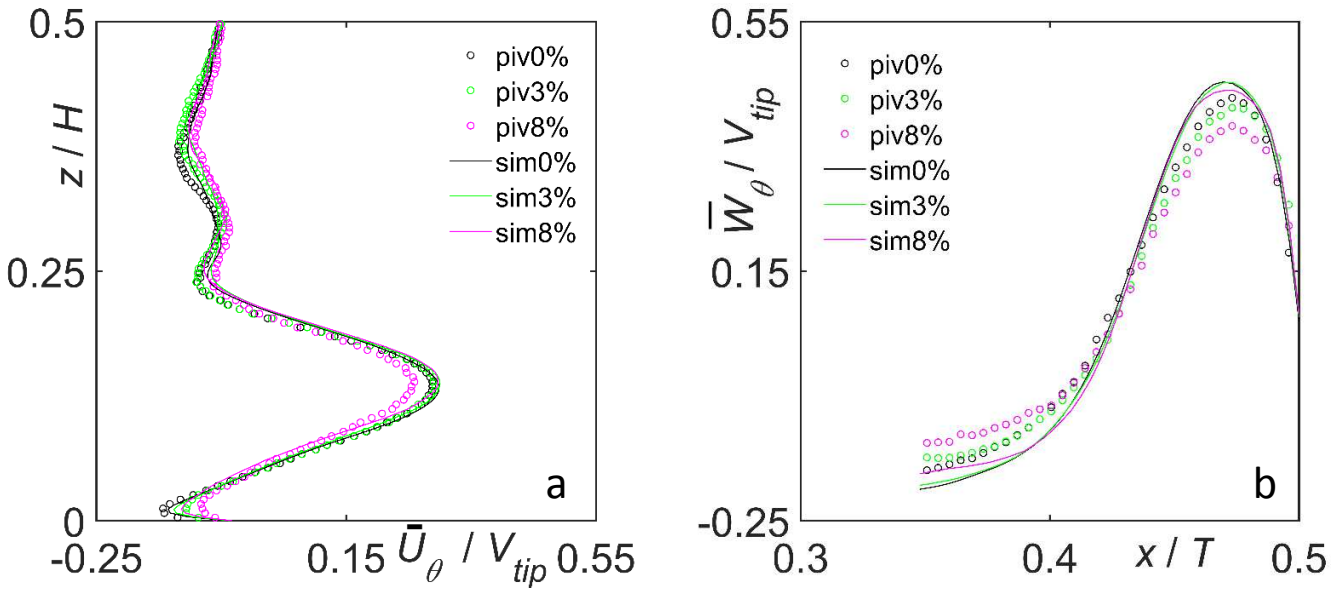

Fig. 11. (a) Vertical profile of normalized mean radial velocity at *x/T* = 0.45 for different solids volume fractions 0%, 3% and 8% at impeller angle θ = 60°; (b) Horizontal profile of normalized mean axial velocity at *z/H* = 0.25 for different solids volume fractions: 0%, 3% and 8% at impeller angle θ = 60°.

In this section, the effect of solids volume fractions on the liquid impeller-angle-resolved mean velocity and TKE will be discussed. The overall, average flow pattern in the field of view of the PIV experiments is shown in Figure 10 for all the tank-averaged solids volume fractions covered in this work. We see a downward inclined liquid stream coming off the impeller that impacts on the lower part of the side wall. Most of the liquid is diverted upward along the side wall. Liquid than circulates in the upper regions of the tank and returns to the impeller. The most striking effect of the particles that is captured by experiment as well as simulation is the reduction of liquid flow underneath the impeller as a result of hindrance by the particles as the solids volume fraction increases. The distribution of colors in Figure 10 demonstrates a good quantitative agreement between experiment and simulation when it comes to the average velocity magnitude (in the plane of view) and its spatial distribution. Closer inspection, however, shows that the reduction of velocity magnitude with increasing solids volume fraction as consistently measured in the experiments is hardly observed in the simulations. To better quantify this disagreement between experiment and simulation, velocity profiles have been plotted in Figure 11. These profiles have been chosen so as to capture the major peak velocity values: Figure 11a captures the strong radial velocity in the impeller outstream; Figure 11b the strong vertical stream along the side wall of the tank. Where there is a good match between experiment and simulation in terms of the shape of the velocity profiles, the reduction of radial and axial peak velocity values by 12% and 11% respectively when going from the single-phase case to the 8% solids volume fraction case in the experiments is hardly

observed in the simulations in which the reduction is 3% for both radial and axial peak velocity values. The reason for this mismatch is not fully clear. Solids and liquid in the simulations are fully coupled, in terms of excluded volume, as well as when it comes to the forces and torques the particles exert on the liquid (and vice versa). It might be that the spatial resolution (9.6 grid spacings per sphere diameter) is not sufficiently high to resolve the flow around the particles. Particularly in the impeller outstream where particle-based Reynolds numbers can reach levels well above 10^2 more resolution is required.

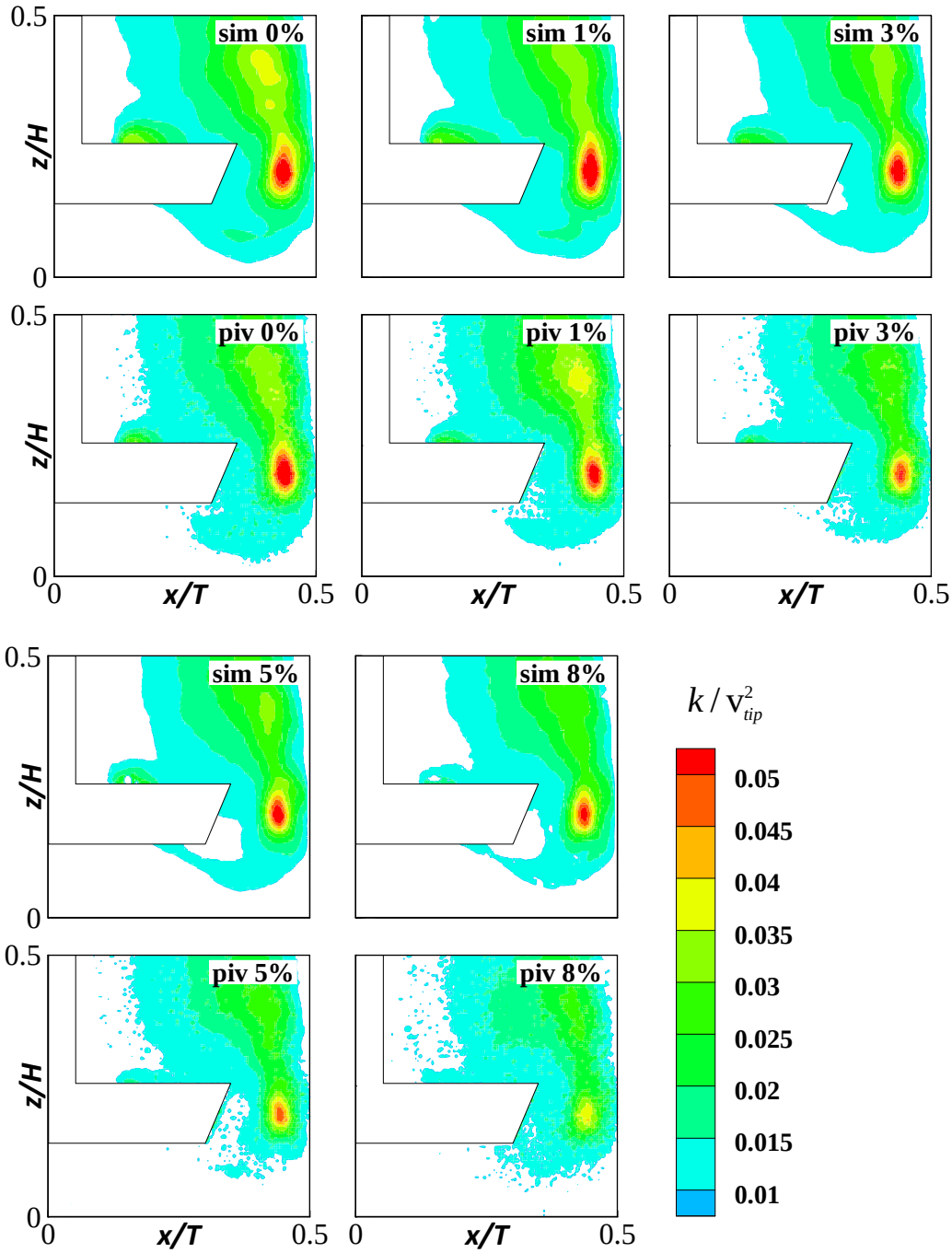

Fig. 12. Normalized turbulent kinetic energy contours of the liquid for different solids volume fractions: 0%, 1%, 3%, 5% and 8% at impeller angle $\theta = 60^{o}$.

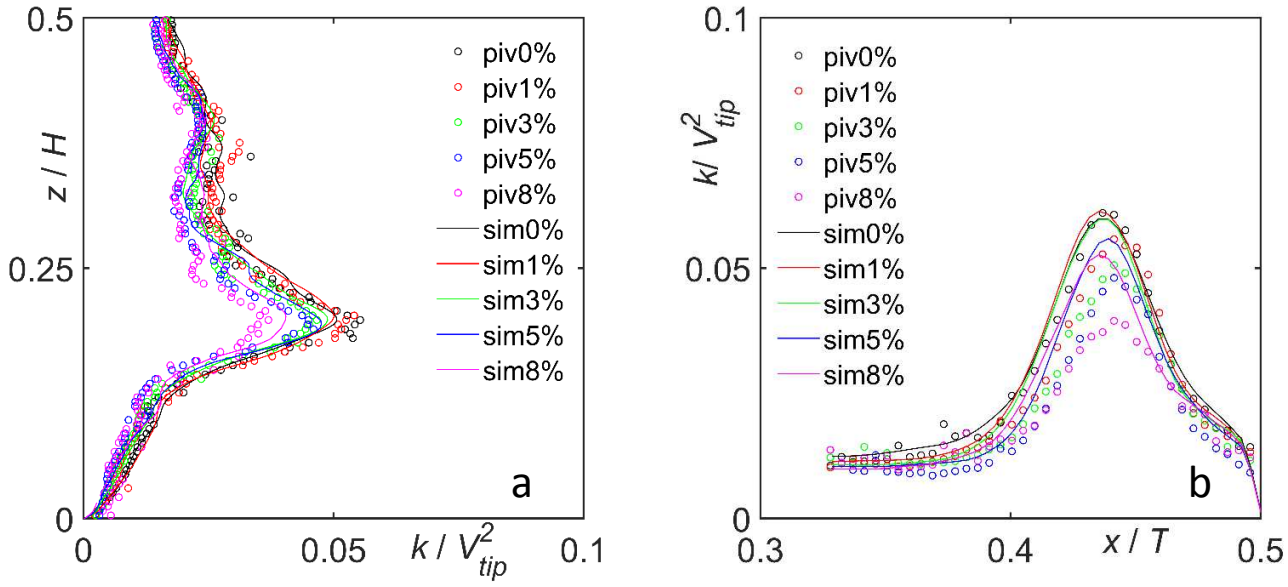

Fig. 13. (a) Vertical profile of normalized turbulent kinetic energy of the liquid at x/T = 0.45 for different solids volume fractions 0%, 1%, 3%, 5% and 8% at impeller angle θ = 60°; (b) Horizontal profile of normalized turbulent kinetic energy of the liquid at z/H = 0.2 for different solids volume fractions 0%, 1%, 3% 5% and 8% at impeller angle θ = 60°.

Finally, we present the fluctuation levels of the liquid velocities, which are only caused by erratic fluid motion brought about by particles as well as turbulence generated by the impeller. This is because our velocity measurements were done for a specific angle of the impeller with the measurement plane so that the fluctuations due to periodic impeller motion are not part of the velocity fluctuations measured. Figure 12 shows both the simulated and experimental TKE values of the liquid, which were calculated only based on axial and radial velocity components. As we can see, TKE hotspots emerge in the impeller discharge region. In the simulations, the peak values of TKE reduce significantly with an increase of the number of particles present in the tank. The decay of TKE in the experiments is, however, stronger so that also in terms of TKE the simulations underestimate the damping of liquid flow due to the presence of solids. Turbulence attenuation due to particles is in accordance with the previous investigations in Li et al. (2018), Unadkat et al. (2009) and Gabriele et al. (2011).

A more quantitative assessment of the levels of turbulence attenuation is given in Figure 13. Here we show profiles that indicate the peak TKE values. In contrast to Figure 11, that hardly shows an effect of the particles on simulated average velocity components, we now do see significant damping in the simulations. Where experimental TKE peak levels reduce by some 39% from 0% to 8% solids, simulated peak levels reduce by 21%. The width and shape of TKE peaks agrees reasonably well between simulation and experiment.

5. Conclusions

The 2D-PIV technique combined with the refractive index matching method has been used to simultaneously measure flow velocity and solids concentration in a stirred tank in the transitional flow regime for the first time. The flow around individual particles is well resolved so that it is possible to study how the particles affect the flow fields in detail.

Particle-resolved simulations with LB method have been performed to mimic the same solids suspension processes as in the PIV experiments. The flow fields including those around the particles have been fully resolved except for the flow in the gap between closely spaced particles where a lubrication force model has been applied. The simulation depicts the whole process of solid-liquid suspension in the stirred stank from the initial state and it shows that most of the particles are suspended and mixed throughout the whole tank after twenty impeller revolutions.

The novelty of this paper lies in confronting numerical results with experimental ones. For the first time, particle-resolved measurements and simulations are compared for an identical solid-liquid flow system operating under the same conditions. Given the high solids loading (up to 8% by volume), the conditions are very challenging from an experimental as well as from a computational perspective. Careful refractive index matching is required in the experiment, whereas the simulations require high resolution in space and time.

The simulated results are in good agreement with the experimental data in terms of both the instantaneous and averaged solids distributions in the stirred tank. Particle concentrations are high underneath the impeller, which was expected based on preliminary estimates of the just-suspended impeller speed for this solid-liquid system. In addition, solids concentrations are also relative high in the corner of the tank as well as the near-wall region.

The distributions of the averaged liquid velocities and the turbulent fluctuation levels of the liquid (presented as TKE in this study) in the experiments and simulations also match quite well. The experimental results show that the presence of particles significantly attenuates the liquid average velocities as well as the TKE levels. The simulated TKE values show the same trend with, however, somewhat weaker attenuation. The simulations do not show significant attenuation of the average liquid velocities.

Investigating the latter discrepancy thus is a major direction for future research. Also extending the experimental procedures so that also particle velocities can be measured simultaneously with liquid velocity is a priority.

Acknowledgment

The financial supports from the National Key R&D Program of China (2017YFB0306703) and the National Natural Science Foundation of China (No.21676007) are gratefully acknowledged.

Literature cited

Angst, R., Kraume, M., 2006. Experimental investigations of stirred solid/liquid systems in three different scales: Particle distribution and power consumption. Chem. Eng. Sci. 61, 2864-2870.

Atherton, T.J., Kerbyson, D.J., 1999. Size invariant circle detection. Image. Vision. Comput. 17, 795-803.

Baldi, G., Conti, R., Alaria, E., 1978. Complete suspension of particles in mechanically agitated vessels. Chem. Eng. Sci. 33, 21-25.

Bittorf, K.J., Kresta, S.M., 2003. Prediction of cloud height for solid suspensions in stirred tanks. Chem. Eng. Res. Des. 81, 568-577.

Carletti, C., Montante, G., Westerlund, T., Paglianti, A., 2014. Analysis of solid concentration distribution in dense solid-liquid stirred tanks by electrical resistance tomography. Chem. Eng. Sci. 119, 53-64.

Chen, S., Doolen, G.D., 1989. Lattice Boltzmann method for fluid flows. Annu. Rev. Fluid. Mech. 30, 329-364.

Christensen, K.T., 2004. The influence of peak-locking errors on turbulence statistics computed from PIV ensembles. Exp. Fluids. 36, 484-497.

Derksen, J.J., Van den Akker, H.E.A., 1999. Large-eddy simulations on the flow driven by a Rushton turbine. AIChE J. 45, 209-221.

Derksen, J.J., 2003. Numerical Simulation of Solids Suspension in a Stirred Tank. AIChE J. 49, 2700-2714.

Derksen, J.J., 2006. Long-time solids suspension simulations by means of a large-eddy approach. Chem. Eng. Res. Des. 84, 38-46.

Derksen, J.J., Sundaresan, S., 2007. Direct numerical simulations of dense suspensions: wave instabilities in liquid-fluidized beds. J. Fluid. Mech. 587, 303-336.

Derksen, J.J., 2009. Solid particle mobility in agitated Bingham liquids. Ind. Eng. Chem. Res. 48, 2266-2274.

Derksen, J.J., 2011. Simulations of granular bed erosion due to laminar shear flow near the critical Shields number. Phys. Fluids. 23,113303.

Derksen, J.J., 2012. Highly resolved simulations of solids suspension in a small mixing tank. AIChE J. 58, 3266-3278.

Derksen, J.J., 2014a. Simulations of solid-liquid scalar transfer for a spherical particle in laminar and turbulent flow. AIChE J. 60, 1202-1215.

Derksen, J.J., 2014b. Simulations of solid-liquid mass transfer in fixed and fluidized beds. Chem. Eng. J. 255, 233-244.

Derksen, J.J., 2018. Eulerian-Lagrangian simulations of settling and agitated dense solid-liquid suspensions-achieving grid convergence. AIChE J. 64, 1147-1158.

Eggels, J.G.M., Somers, J.A., 1995. Numerical simulation of free convective flow using the lattice-Boltzmann scheme. Int. J. Heat. Fluid. Flow. 16, 357-364.

Eswaran, V., Pope, S.B., 1988. An examination of forcing in direct numerical simulations of turbulence. Comput. Fluids. 16, 257-278.

Feng, Y., Goree, J., Liu, B., 2011. Errors in particle tracking velocimetry with high-speed cameras. Rev. Sci. Instrum. 82, 053707.

Gabriele, A., Tsoligkas, A., Kings, I., Simmons, M., 2011. Use of PIV to measure turbulence modulation in a high throughput stirred vessel with the addition of high Stokes number particles for both up-and down-pumping configurations. Chem. Eng. Sci. 66, 5862-5874.

Goldstein, D., Handler, R., Sirovich, L., 1993. Modeling a no-slip flow boundary with an external force field. J. Comp. Phys. 105, 354-366.

Guha, D., Ramachandran, P.A., Dudukovic, M.P., 2007. Flow field of suspended solids in a stirred tank reactor by Lagrangian tracking. Chem. Eng. Sci. 62, 6143-6154.

Guida, A., Fan, X., Parker, D., Nienow, A., Barigou, M., 2009. Positron emission particle tracking in a mechanically agitated solid-liquid suspension of coarse particles. Chem. Eng. Res. Des. 87, 421-429.

Guida, A., Nienow, A.W., Barigou, M., 2010. PEPT measurements of solid-liquid flow field and spatial phase distribution in concentrated monodisperse stirred suspensions. Chem. Eng. Sci. 65, 1905-1914.

Guiraud, P., Costes, J., Bertrand, J., 1997. Local measurements of fluid and particle velocities in a stirred suspension. Chem. Eng. J. 68, 75-86.

Harrison, S.T., Stevenson, R., Cilliers, J.J., 2012. Assessing solids concentration homogeneity in Rushton-agitated slurry reactors using electrical resistance tomography (ERT). Chem. Eng. Sci. 71, 392-399.

Hosseini, S., Patel, D., Ein-Mozaffari, F., Mehrvar, M., 2010. Study of solid-liquid mixing in agitated tanks through electrical resistance tomography. Chem. Eng. Sci. 65, 1374-1384.

Khan, F., Rielly, C., Brown, D., 2006. Angle-resolved stereo-PIV measurements close to a down-pumping pitched-blade turbine. Chem. Eng. Sci. 61, 2799-2806.

Kim, S., Karrila, S.J., 1991. Microhydrodynamics: principles and selected applications. Butterworth-Heinemann, Boston.

Li, G., Gao, Z., Li, Z., Wang, J., Derksen, J.J., 2018. Particle-resolved PIV experiments of solid-liquid mixing in a turbulent stirred tank. AIChE J. 64, 389-402.

Liu, Xin., Bao, Y., Li, Z., Gao, Z., 2010. Analysis of turbulence structure in the stirred tank with a deep hollow blade disc turbine by time-resolved PIV. Chinese. J. Chem. Eng. 18, 588-599.

MathWorks Inc., 2016. Imfindcircles documentation. http://uk.mathworks.com/help/images/ref/imfindcircles.html/ (accessed 16 July 2016).

Micheletti, M., Yianneskis, M., 2004. Study of fluid velocity characteristics in stirred solid-liquid suspensions with a refractive index matching technique. P. I. Mech. Eng. E-J. Pro. 218, 191-204.

Mo, J., Gao, Z., Bao, Y., Li, Z., Derksen, J.J., 2015. Suspending a solid sphere in laminar inertial liquid flow-experiments and simulations. AIChE J. 61, 1455-1469.

Moin, P., Mahesh, K., 1998. Direct numerical simulation: a tool in turbulence research. Annu. Rev. Fluid. Mech. 30, 539-578.

Montante, G., Paglianti, A., Magelli, F., 2012. Analysis of dilute solid-liquid suspensions in turbulent stirred tanks. Chem. Eng. Res. Des. 90, 1448-1456.

Nguyen, N.Q., Ladd, A.J.C., 2002. Lubrication corrections for lattice-Boltzmann simulations of particle suspensions. Phys. Rev. E. 66, 046708.

Nienow, A.W., 1968. Suspension of solid particles in turbine agitated baffled vessels. Chem. Eng. Sci. 23, 1453-1459.

Paul, E.L., Atiemo-Obeng, V.A., Kresta, S.M., 2004. Handbook of Industrial Mixing: Science and Practice. John Wiley & Sons, New York.

Sardeshpande, M.V., Juvekar, V.A., Ranade, V.V., 2011. Solid suspension in stirred tanks: UVP measurements and CFD simulations. Can. J. Chem. Eng. 89, 1112-1121.

Sharma, R., Shaikh, A., 2003. Solids suspension in stirred tanks with pitched blade turbines. Chem. Eng. Sci. 58, 2123-2140.

Somers, J.A., 1993. Direct simulation of fluid flow with cellular automata and the lattice-Boltzmann equation. Appl. Sci. Res. 51, 127-133.

Succi, S., 2001. The lattice Boltzmann equation for fluid dynamics and beyond. Clarendon Press, Oxford.

Tahvildarian, P., Ng, H., D'amato, M., Drappel, S., Ein-Mozaffari, F., Upreti, S.R., 2011. Using electrical resistance tomography images to characterize the mixing of micron-sized polymeric particles in a slurry reactor. Chem. Eng. J. 172, 517-525.

Ten Cate, A., Nieuwstad, C.H., Derksen, J.J., Van den Akker, H.E.A., 2002. PIV experiments and lattice-Boltzmann simulations on a single sphere settling under gravity. Phys. Fluids. 14, 4012-4025.

Tennekes, H., Lumley, J., 1973. A first course in turbulence. MIT Press, Cambridge.

Unadkat, H., Rielly, C.D., Hargrave, G.K., Nagy, Z.K., 2009. Application of fluorescent PIV and digital image analysis to measure turbulence properties of solid-liquid stirred suspensions. Chem. Eng. Res. Des. 87, 573-586.

Virdung, T., Rasmuson, A., 2007a. Solid-liquid flow at dilute concentrations in an axially stirred vessel investigated using particle image velocimetry. Chem. Eng. Commun. 195, 18-34.

Virdung, T., Rasmuson, A., 2007b. Measurements of continuous phase velocities in solid-liquid flow at elevated concentrations in a stirred vessel using LDV. Chem. Eng. Res. Des. 85, 193-200.

Yamamoto, Y., Potthoff, M., Tanaka, T., Kajishima, T., Tsuji, Y., 2001. Large-eddy simulation of turbulent gas-particle flow in a vertical channel: effect of considering inter-particle collisions. J. Fluid. Mech. 442, 303-334.

Zhang, Y., Gao, Z., Li, Z., Derksen, J. J., 2017. Transitional Flow in a Rushton Turbine Stirred Tank. AIChE J. 63, 3610-3623.

Zwietering, T.N., 1958. Suspending of solid particles in liquid by agitators. Chem. Eng. Sci. 8, 244-253.